Contactless Air–Filled Substrate Integrated Waveguide on Low–Cost PCB for D–Band Applications

Contactless Air–Filled Substrate Integrated Waveguide on Low–Cost PCB for D–Band Applications

Kaan Aktaş, *Student Member, IEEE*, Martin Petek, *Member, IEEE*, Enrico Tolin, Simona Bruni, Jorge A. Tobón Vásquez, Francesca Vipiana, *Senior Member, IEEE*

***Abstract*—D-band radar systems offer significant advantages for automotive applications, including large bandwidth for high-precision object detection in crowded environments and compact solutions. However, their widespread adoption is hindered by significant transmission losses and high manufacturing costs in conventional transmission line technologies. This paper addresses these challenges by introducing a novel, cost-effective contactless air-filed substrate integrated waveguide (CLAFSIW) design for the 134-148.5 GHz frequency range. It features an E-bend vertical transition allowing for compact integration with next generation monolithic microwave integrated circuit radars. Fabricated using a standard FR4 printed circuit board, the design is suitable for mass production. The prototype board demonstrate an excellent performance close to simulation predictions despite manufacturing discrepancies. Measurements confirm an average insertion loss of 0.037 dB/mm with a back-to-back transition matching below -10 dB across the desired band. The design also exhibits high isolation, with crosstalk between adjacent CLAFSIW lines remaining below -26 dB.**

***Index Terms*—Automotive applications, D-band, electromagnetic band gap, gap waveguide, millimeter wave radar, microwave bends, microwave integrated circuits, periodic structures, transmission lines.**

I. Introduction

WIDEBAND compact radar systems are becoming critical for emerging advanced driver assistance systems (ADAS), offering two key benefits: resilience to environmental conditions (temperature, air currents, darkness, etc.) [1], and high-resolution object detection with richer data for enhanced artificial intelligence shape recognition [2], [3]. Within the latter scope, the $76-81$ GHz band has been introduced in Europe and the United States to replace the traditional 24 GHz ultra-wideband [4]. However, due to increasing number of radar implementations in newer vehicles, it is expected that this new band will be soon congested, hence increasing the interference from other radar systems operating in the same frequency range [5]. Consequently, the D-band is being actively investigated in Europe, with potential frequency allocations spanning $122.25-130$ GHz, $134-141$ GHz, and $141-148.5$ GHz [6].

Manuscript received ; revised

This publication is supported in part by the Horizon Europe Research and Innovation Program under the GENIUS Project (GA101072560) and in part by the project MedWaveImage funded by Interreg Central Europe (CE0200670). *(Corresponding author: Francesca Vipiana).*

Kaan Aktaş is with the Department of Electronics and Telecommunications, Politecnico di Torino, 10129 Torino, Italy, and also with with IMST GmbH, 47475 Kamp-Lintfort, Germany (emails: kaan.aktas@polito.it, kaan.aktas@imst.de).

Martin Petek, Jorge Alberto Tobón Vásquez and Francesca Vipiana are with the Department of Electronics and Telecommunications, Politecnico di Torino, 10129 Torino, Italy (emails: martin.petek@polito.it, jorge.tobon@polito,it, francesca.vipiana@polito.it).

Enrico Tolin and Simona Bruni are with IMST GmbH, 47475 Kamp-Lintfort, Germany (emails: enrico.tolin@imst.de, simona.bruni@imst.de).

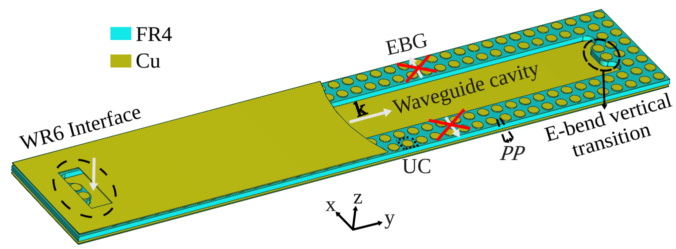

Fig. 1. Conceptual illustration of the proposed D-band CLAFSIW design. Dashed black line: WR6 aperture and E-bend vertical transition. Silver arrow: direction of the wave vector **k**. Red cross: propagation cancellation in any direction. Yellow: Copper (Cu). Blue: FR4 substrate. Pad-to-pad distance (PP). Dotted square: Unit cell (UC).

Operating at D-band offers more compact and larger bandwidth antenna designs leading to higher precision in distinguishing targets in crowded environments [3], [7]. Although D-band offers significant advantages, traditional transmission line technologies encounter substantial performance limitations at these frequencies. The demand for cost-effective solutions in the automotive industry presents also a key challenge. Waveguides, despite their low loss characteristics [8], suffer from costly production due to their small size and the need for diffusion bonding to prevent signal leakage from gaps [9], [10]. Additive manufacturing provides a cost-effective alternative [11], [12]; nevertheless, achieving industrial-scale mass production remains a challenge. Microstrip lines, while offering a cheaper solution using printed circuit board (PCB) fabrication, the dielectric itself introduces additional loss. Furthermore, at higher frequencies, they incur radiation loss caused by fringing fields and surface currents. This not only degrades efficiency but also exacerbates crosstalk [10], [13], [14]. Among other PCB technologies, substrate integrated waveguides (SIW), utilizing closely spaced vias to emulate metallic walls, offer a lower radiation loss. Although well-established in D-band applications [15]–[19], achieving higher transmission requires costly low-loss dielectric materials for the substrate [20]. These dielectric losses may be mitigated by using an air-filled SIW (AFSIW). However, ensuring perfect contact between the metallic plates and the substrate requires complex methods using laser cutting or soldering [21], [22].

A promising alternative is gap waveguide technology [9], as it offers the advantage of diminished radiation and dielectric loss, even with non-uniform gap formation within their structure. Metallic gap waveguides in D-band applications are most commonly based on either pin [23]–[28] or holey electromagnetic bandgap (EBG) structures [29].

While metallized plastic injection molding is an existing low-cost industrial option [30], PCB-based implementations offer direct integration with circuit components. Within PCB-based gap waveguide designs, substrate integrated hole (SIH) unit cells [31]–[33] and mushroom-type unit cells can be used as EBG structures [34]–[40]. Existing gap waveguide designs of both types generally operate at lower frequencies, with very limited literature available in the D-band range. To the best of authors' knowledge, there is no practical implementation of a PCB-based gap waveguide functioning at D-band. Only in [41], a D-band unit cell is proposed for flange leakage suppression. However, this unit cell is constructed on a three-layer PCB. This conflicts our objective of avoiding multilayer solutions, as it significantly increases fabrication complexity compared to a double layer PCB design with a single laminate.

The key novelty of this paper is the introduction of the first D-band gap waveguide based on standard PCB manufacturing. The proposed design in Fig. 1 demonstrates, to the best of authors' knowledge, for the first time a solution using FR4 material to bridge the gap between stringent D-band performance requirements and low-cost, mass-production scalability [1] within the existing PCB standards of automotive industry. As automotive radars transition toward Sub-THz frequencies, maintaining compatibility with conventional PCB processes is critical for commercial viability. This industrial requirement drives the selection of FR4 substrate over costly, specialized microwave substrates [42]–[44]. Despite the challenges of its high dielectric loss, frequency-dependent material properties, and PCB fabrication tolerances at D-band, our design manages these limitations and provides a wide band transmission line specifically targeting the $134 - 148.5$ GHz frequency range. It presents a suitable solution for interconnects and feed networks of radar front-ends established in EBG [23]–[26], [45] and SIW structures [15]–[18].

Unlike SIH unit cells, which requires a high number of vias to define a hole perimeter (potentially complicating design and manufacturing), the proposed EBG design adapts the mushroom-type unit cell of the contactless, air-filled SIW (CLAFSIW). This type of unit cell offers a significant advantage for achieving higher frequency operation due to its minimal periodicity, realized by a central via surrounded by a dielectric. While previously demonstrated at lower frequencies [35]–[38], this work presents the first successful implementation of CLAFSIW to the D-band, within the constraints of conventional manufacturing and high dielectric losses. In addition, its stopband has been characterized through the application of the multimodal transfer matrix method (MMTMM). This method allows to evaluate the stopband attenuation which is not currently available in commercial eigenmode solvers [46]–[49].

Furthermore, we incorporate an E-bend vertical transition into our CLAFSIW design for its compatibility with the waveguide launchers used in current automotive radar microchips [44], [45], [50]. Our via-based solution allows for a design on a single laminate providing better adaptability for mass production compared to multilayer solutions [15]–[17].

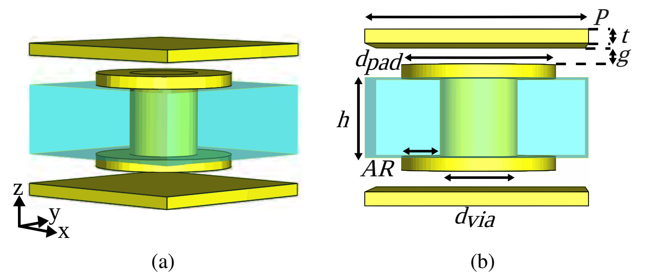

Fig. 2. Unit cell design and parameters: periodicity (P), annular ring width (AR), pad diameter (d_{pad}), via diameter (d_{via}), substrate height (h), gap size (g) and copper thickness (t).

TABLE I
UNIT CELL DESIGN PARAMETERS AND DIMENSIONS WITHIN FABRICATION CONSTRAINTS

Parameters (μm)	Min	Max	Final
P	500	673	560
PP	100	273	160
AR	100	186.5	100
d_{pad}	400	573	400
d_{via}	200	373	200
g	0	50	50

In the context of this study, however, this transition serves only as a characterization interface for measurements, specifically designed to provide a stable and repeatable connection between the CLAFSIW and the measurement equipment.

The paper is organized as follows. Section II introduces the proposed unit cell, including its dispersion diagram and MMTMM analysis. It then details the vertical transition-integrated straight CLAFSIW line and its performance, specifically targeting the $134-148.5$ GHz band for radar microchip applications. Section III describes the prototype realization and the through-reflect-line (TRL) calibration measurements and coupling characteristics. Finally, Sect. IV concludes the paper and outlines future perspectives.

II. CLAFSIW DESIGN AND ANALYSIS

A. Unit cell design and parametric study

In this sub-section, we analyze the stopband sensitivity of a double-sided mushroom-type unit cell, shown in Fig. 2 considering fabrication tolerances at $134 - 148.5$ GHz range. The design is implemented with a $200\,\mu$m thick Panasonic FR4 substrate ($\epsilon_r = 4.7$ and tan$\delta = 0.01$) [51] using standard $35\,\mu$m copper cladding. A $50\,\mu$m air gap is considered to account for maximum anticipated assembly tolerance between the pads and parallel plates [38]. Unlike square pads [35], circular shapes are used to minimize the capacitance effect, hence reaching higher frequencies.

The unit cell is arranged in a square lattice with a sub-wavelength periodicity to achieve a compact design. To balance compactness with the PCB manufacturing limitations (e.g., pad spacing and dimensions), the periodicity is determined by $\lambda_g/4 < P < \lambda_g/3$ at 148.5 GHz. With unit cell

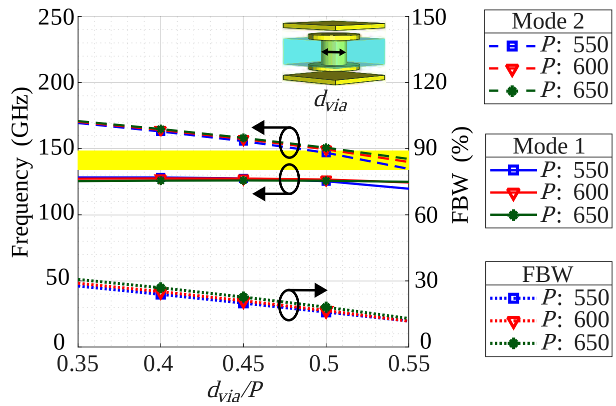

Fig. 3. Unit cell dispersion diagram and fractional bandwidth of the stopband regarding varying via diameter/period ratios for a range of periods. Yellow rectangle highlights the $134 - 148.5$ GHz range. h: 200 μm, g: 50 μm, AR: 100 μm. Inset: unit cell.

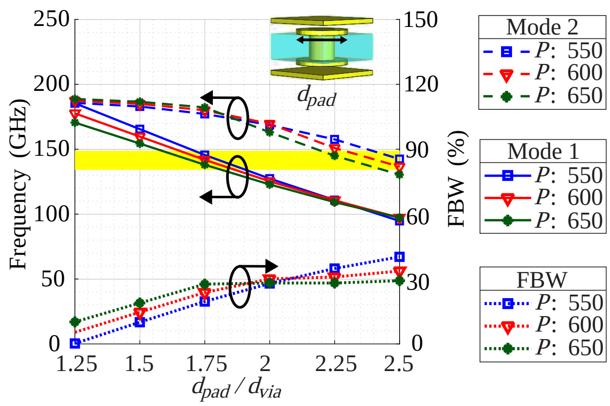

Fig. 4. Dispersion diagrams at d_{via}: 200 μm, h: 200 μm, g: 50 μm. (a) varying circular pad/via diameter ratios at different periods including fractional bandwidth. Yellow rectangle depicts the $134 - 148.5$ GHz range. Inset: unit cell.

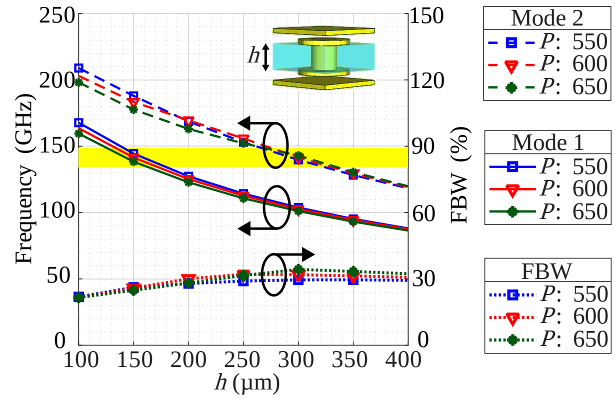

Fig. 5. Dispersion diagram for various substrate heights at different periods including fractional bandwidth. Yellow rectangle indicates the 134-148.5 GHz band. Inset: unit cell. d_{via}: 200 μm, d_{pad}: 400 μm, g: 50 μm.

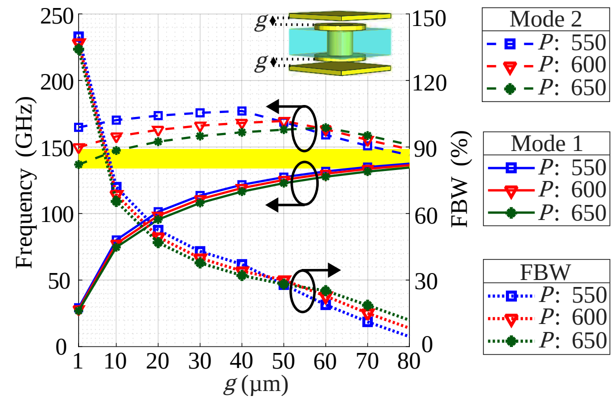

Fig. 6. Dispersion diagram for various gap sizes across a range of periods including fractional bandwidth. Yellow rectangle shows the 134-148.5 GHz range. Inset: unit cell. h: 200 μm, d_{via}: 200 μm, d_{pad}: 400 μm.

dimensions in Table I we now investigate the impact of key parameters on the unit cell's performance for various periods. For each case, we use an eigenmode solver to determine the boundary modes of the stopband (mode 1 and 2), and calculate the fractional bandwidth (FBW).

For minimal radiation loss in CLAFSIW technology an approximate 50% via diameter to period ratio is suggested in [35]. However, this requirement leads to a barely sufficient stopband for the desired band as shown in Fig. 3, resulting in greater sensitivity to manufacturing variations. Consequently, the smallest achievable via diameter (200 μm) is selected to maximize the stopband and enhance tolerance to variations in gaps and pad sizes.

As shown in Fig. 4, the stopband center frequency (f_c) is inversely proportional to pad size, explained with the LC resonance model in [34]. The target stopband is maintained for pad diameters between 380 μm to 440 μm ($1.9 < d_{pad}/d_{via} < 2.2$), highlighting high sensitivity to PCB manufacturing tolerances. For a smaller periodicity, the bandwidth changes at a higher rate within this range. To illustrate these trends, Fig. 4 includes parameter values exceeding the Table I constraints.

Figure 5 demonstrates that the substrate height, h, can be used as a tuning parameter to shift the stopband central frequency without significantly degrading the bandwidth like other parameters. For this design, h is fixed at a standard 200 μm, though sensitivity analysis confirms the stopband remains compliant even with $\pm 10\%$ height variations. While this thickness is at the lower end of conventional FR4 laminate profiles, it is essential to operate at D-band range and still provides a cheaper solution than using specialized RF materials [45].

As shown in Fig. 6, the stopband bandwidth decreases with increasing gap size (g). Since the gap size is expected to be non-uniform across the assembled structure, the 550 μm period is advantageous to ensure the largest fractional bandwidth and also a compact design.

The finalized unit cell dimensions (see Table I) are adapted for integration of the subsequent vertical transitions and matching performance by adjusting the period and the pad diameter to 560 μm and 400 μm respectively (see Sect. II-B). To gain a complete understanding of the unit cell stopband properties we use the MMTMM [49] with the first nine modes per port. Following the recommendations in [49], we define the computational domain used with the MMTMM as in the inset

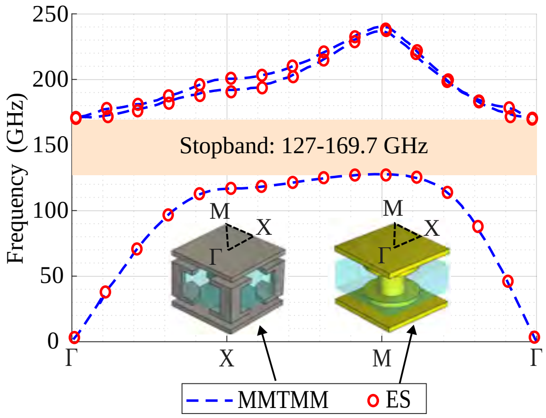

(a)

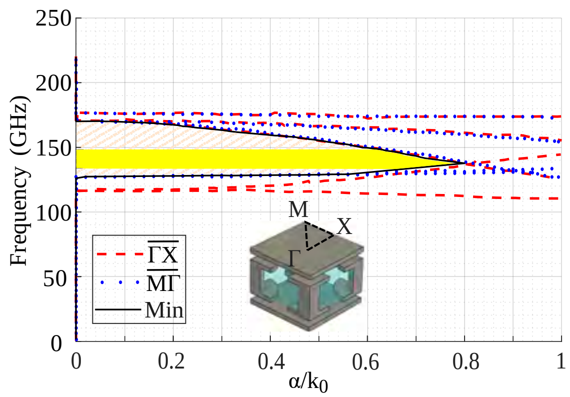

(b)

Fig. 7. Analysis of the proposed unit cell from different Brillouin zone perspectives, used for eigenmode solver (ES) and MMTMM calculations within the same lattice. (a) Full dispersion diagram for the first three modes with stopband highlighted between mode 1 and 2 with an orange rectangle (b) Normalized attenuation constant achieved with MMTMM for the $\overline{\Gamma X}$, $\overline{M\Gamma}$ regions. Black outline and orange diagonal lines highlight the minimum attenuation region in any direction. Yellow region denote the 134-148.5 GHz frequency range.

of Fig. 7.

Real-valued solutions show excellent agreement between the eigenmode solver and the MMTMM in Fig. 7(a) confirming a stopband from 127 to 169.7 GHz with 28.8 % FBW. Stopband attenuation analysis in Fig. 7(b) reveals a sharp increase above 127 GHz, with normalized attenuation values reaching $0.63-0.8$ across all propagation directions within the operational band. Therefore, we expect the EBG structure to effectively suppress leakage within 2-3 rows as demonstrated in a previous work [47].

B. Straight CLAFSIW design with E-bend vertical transition

The proposed CLAFSIW concept is illustrated in Fig. 1. Simulations are performed using FDTD solver of the EMPIRE software [52] by considering a uniform gap size throughout the entire structure. As detailed in Fig. 8(a), the structure features three segments: metallic top and bottom covers and a middle FR4 layer. The top cover incorporates two WR6 waveguide apertures, while the middle layer features a 2-row unit cell frame placed around the waveguide cavity and a vertical transition placed beneath the apertures. A 100 μm edge clearance is maintained between the pads and the waveguide cavity (Fig. 8(b)). This minimum spacing ensures compliance with manufacturing constraints and minimizes the interaction of the wave with lossy substrate.

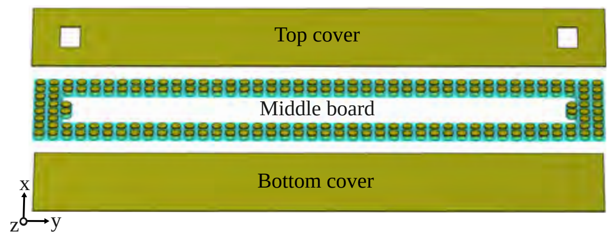

(a)

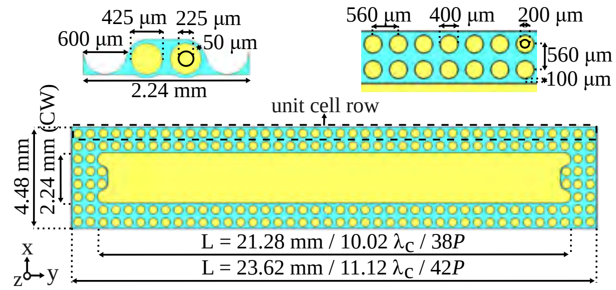

(b)

Fig. 8. Detailed CLAFSIW Structure. (a) Layer-by-layer decomposition. (b) Top view of the middle layer showing waveguide channel, matching structure (top-left), and EBG segment (top-right) with detailed dimensions. Channel width (CW).

To integrate the vertical transition while accommodating 600 μm drilling constraints and optimize CLAFSIW efficiency, the waveguide channel width (CW) is designed larger than standard WR6 dimensions. The simulation in Fig. 9 demonstrates that the configuration with four times the unit cell periodicity maintains the optimal transmission performance across gap sizes of $10-50\,\mu$m, with $|S_{21}| > -0.53$ dB over $10\lambda_c$ segment. Here λ_c is the wavelength at f_c (i.e. 141.25 GHz) of the target band. At $50\,\mu$m gap, the design achieves an average transmission loss of 0.017 dB/mm calculated over this frequency range.

The vertical transition utilizes two vias (see top left of Fig. 8(b)) with a 50 μm clearance, the minimum limit for mechanical drilling. As shown in Fig. 10, this dual-via configuration provides optimal transmission across the $134-148.5$ GHz band. Therefore, to satisfy channel width requirements and drilling tolerances for the transition, the unit cell period is increased from 550 to 560 μm (see Table I), thereby widening the waveguide channel.

Since via dimensions and spacing of the transition are nearly at the minimum of manufacturing limits (see Table I), impedance matching is improved by tuning also the unit cell pad size. Figure 11 compares two CLAFSIW designs using unit cells UC_1 and UC_2 (pad sizes: 425 and 400 μm) while the vertical transition is fixed at a pad size of 425 μm. UC_2 provides superior matching with $|S_{11}| < -10$ dB and $|S_{21}| > -1$ dB while retaining the full stopband coverage over the entire band of interest.

All of these adjustments led to the final CLAFSIW design

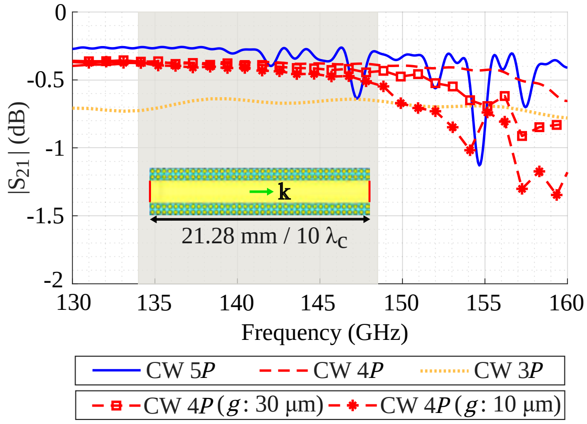

Fig. 9. S_{21} amplitude for varying channel widths (multiples of unit cell periodicity P) at g : 50 μm, with additional gap sizes $(10, 30\,\mu\text{m})$ for the $4P$ width. Grey region indicates the operating band. Inset: $10\lambda_c$ CLAFSIW simulation model fed from the sides using final unit cell dimensions in Table I. Port placements in red rectangles. **k**: wave vector. For all configurations, $|S_{11}| < -19$ dB across $130-160$ GHz.

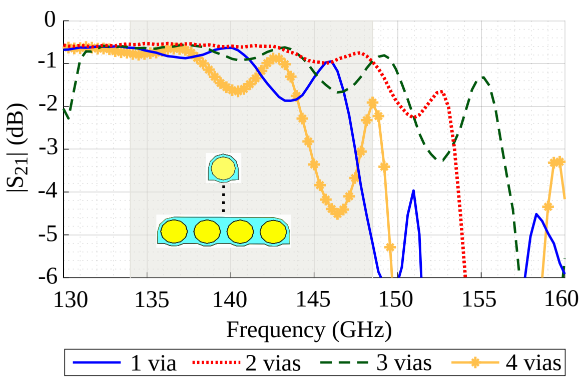

Fig. 10. Comparative analysis of transmission performance for various via quantities in the vertical transition of CLAFSIW design in Fig. 8. Inset depicts vertical transitions with 1 via and 4 vias. g : 50 μm.

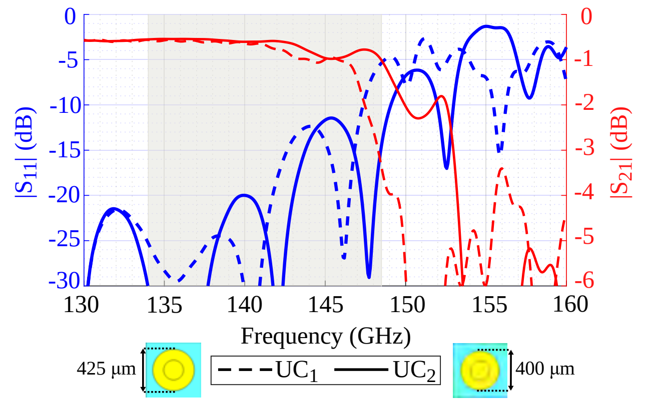

Fig. 11. Matching comparison between mid-band (UC_1) and implemented (UC_2) unit cells having 425 and 400 μm pad diameters respectively. Inset depicts unit cell pad size. g : 50 μm.

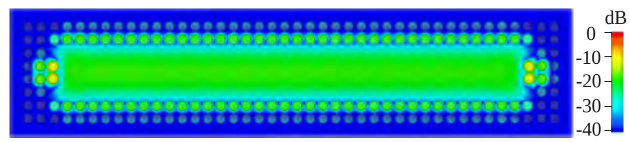

(a) XY plane view at 134 GHz

(b) YZ plane view at 134 GHz

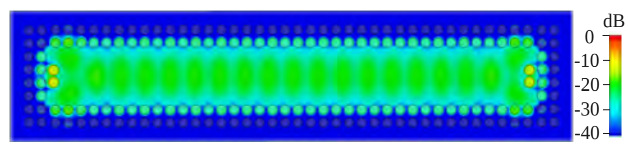

(c) XY plane view at 148.5 GHz

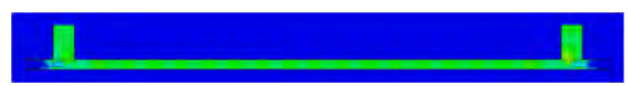

(d) YZ plane view at 148.5 GHz

Fig. 12. Electric field distributions at maximum amplitude with a normalized dB scale shown from top (XY) and side (YZ) plane views.

shown in Fig. 8 with performance indicated in Fig. 11 at 50μm gap for $10\lambda_c$ length. The electric field distributions are presented in Fig. 12, demonstrating the structure effectiveness in performing the vertical transition and mitigating leakage from the gaps, hence effectively confining waves within the waveguide channel with two rows of unit cells only.

III. Prototype Measurements and Discussion

In this section, we experimentally validate and characterize the proposed CLAFSIW design by analyzing its performance across different lengths and applying thru, reflect, line (TRL) de-embedding to understand the associated losses. Note that, in the simulations we consider a uniform gap size across the entire model. Additionally, we examine the suppression of coupling between two adjacent waveguides in relation to the number of unit cells at the intersection. The latter analysis becomes important when multiple CLAFSIWs carrying different signals are fabricated on the same substrate and placed in close proximity.

A. Prototype board organization

We first begin by explaining in detail the organization of the prototype board. It is composed of a stacked configuration of three independent boards: top, middle and bottom. The top and bottom boards are the PCB realization of the top and bottom copper covers in Fig. 8(a). The assembled configuration is shown in Fig. 13, detailing how the components are integrated. Each individual board is a double-sided PCB with bare copper separated by a coating material that maintains a gap. Note that the material does not cover the pads and the waves are significantly attenuated before reaching the coating interface, yielding a negligible impact on CLAFSIW performance. The rectangular copper-plated slot is designed to accommodate the WR6 flange. The three boards are screwed together to constitute the final prototype board. Since the CLAFSIW design is fully enclosed, no additional surface finishing is

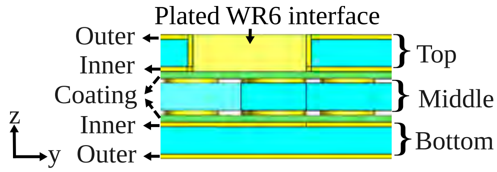

Fig. 13. Side view of the prototype board showing its decomposition.

TABLE II
WAVEGUIDE CHANNEL LENGTHS OF MANUFACTURED DESIGNS

Designs	Length (mm)	Length (λ_c)
T	21.28	10
S	10.42	4.9
L0	24.08	11.3
L1	31.92	15
L2	42.56	20
C	60	28.2
O	10.66	5.02

applied for oxidation.

Each board is divided in three sections as depicted in Fig. 14(a): coupling, 2-row and 3-row designs. The N-row sections contain designs where the waveguide cavity is surrounded by N rows of unit cells, as exemplified in Fig. 8(b) for a 2-row design. The middle board is shown in Fig. 14(a). It includes the waveguide cavities that are formed with a 600 μm drilling tool and all the vias used in EBG structures and vertical transitions. Each design is indicated with an arrow. The T CLAFSIW line, which stands for "thru", is the one explained in Sect. II-B. The L0, L1, L2 lines are straight CLAFSIW designs as T with various lengths. 'L' stands for "Line" and the numbering is just to indicate the shortest to the longest length. The design S (for Short) is intended to provide wave reflection with a load composed of EBG unit cells placed at the end of the CLAFSIW. The Open (O) design is intended for an open circuit, however, it is omitted from our analysis as Short design demonstrated a superior reflection. The number at the subscript of each line is to represent how much unit cell rows are used (i.e. T_2 for 2-rows). Waveguide channel length of each design in terms of wavelength (λ_c) are listed in the Table II. The 3-row designs are structurally identical to 2-row CLAFSIWs, but placed in different orders and uses three unit cell rows to investigate whether an increase in rows influences the confinement of waves within the waveguide cavity. The numbering with white font and black background represents the excitation ports.

On the left side of the board, coupling designs C2, C3, C4 are placed. 'C' stands for "coupling". Each incorporates a pair of intersecting mirrored CLAFSIW designs, and allow to investigate the ability of EBG structures to suppress the unwanted coupling. The numbering represents how much rows of unit cell are used at the intersection.

The inner surface of the top board is depicted in Fig. 14(b). The copper layer is co-plated with the outer surface and then covered with a PCB coating material. The remaining copper shapes, function as the top and bottom covers for the vias and

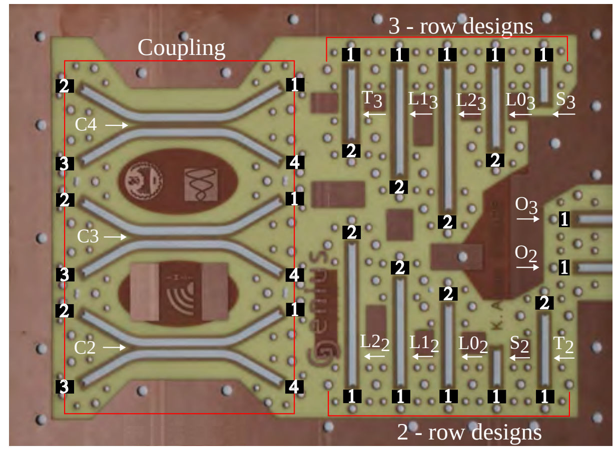

(a)

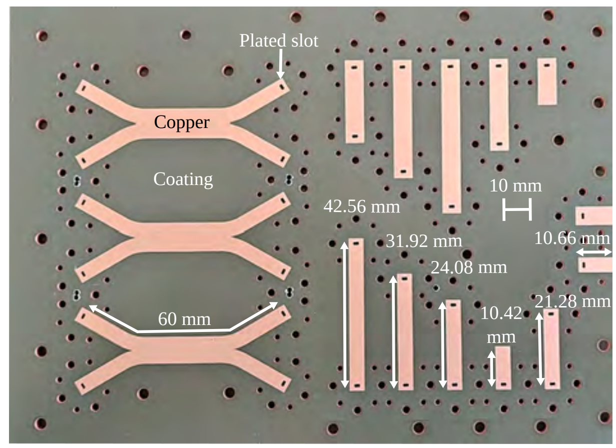

(b)

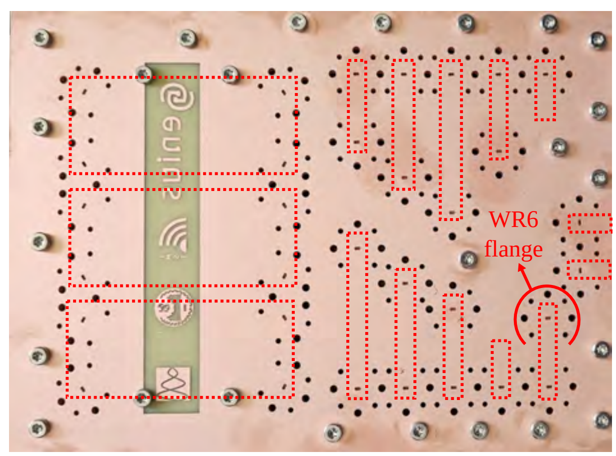

(c)

Fig. 14. Manufactured prototype boards, from middle-to-top board assembly order. (a): middle board scheme with arrows indicating the designs. Through (T), Short (S), Open (O) and Lines (L) with a number indicating increasing length are shown. The subscript indicates the rows of unit cell (two or three). Port numbers are indicated with a white font with black background. Coupling (C) with a number indicating the rows of unit cell at the intersection of two bended and mirrored CLAFSIW designs. (b): top board inner surface and the waveguide cavity length of each design. (c): top board outer surface where each design is highlighted with red dashed rectangles. Semi-circle: WR6 flange mounting holes example.

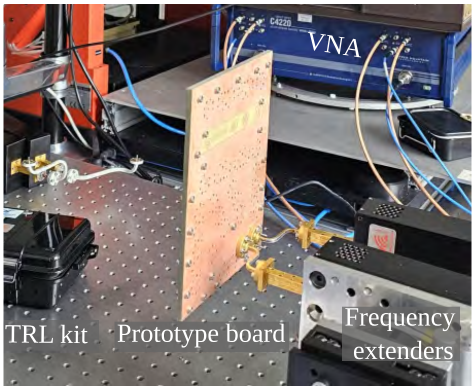

Fig. 15. Measurement setup showing the measurement of the straight CLAFSIW line T_2.

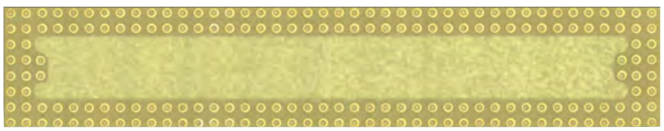

Fig. 16. Optical microscope view of T_2 straight CLAFSIW prototype on the middle board.

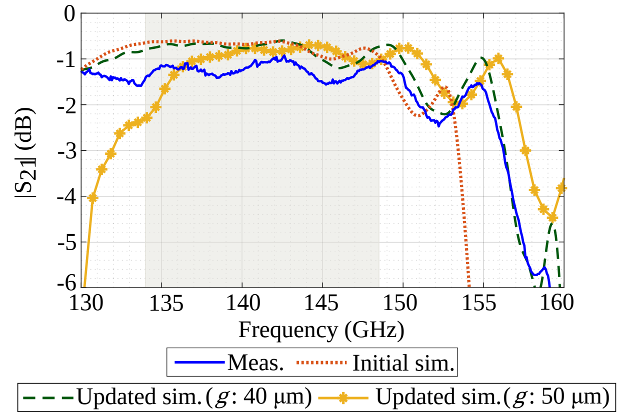

(a)

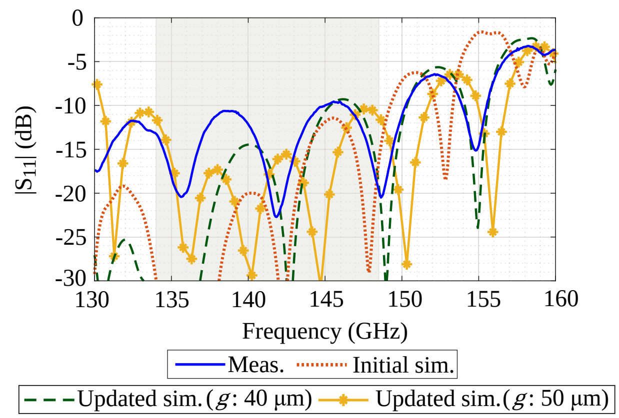

(b)

Fig. 17. Comparison between measurements (meas.) and simulations (sim.): (a) transmission parameters and (b) reflection parameters. The "Initial sim." corresponds to the UC_2 results in Fig. 11. The "Updated sim." accounts for the updated design under prototype dimensions in Table III, assuming a uniform gap size of 40 and 50 μm across the structure.

the cavities on the middle board. This creates the complete CLAFSIW structures and their waveguide channel length is indicated by an arrow.

The outer surface of the top board is depicted in Fig. 14(c). The area where a WR-6 flange is mounted is visible, with its corresponding holes marked by a red semi-circle. Each individual designs are demarcated by red dashed rectangles. Note that the bottom board has the same structure as the top board but is mirrored with respect to z axis and is without the slots.

Each CLAFSIW design on the prototype board is measured using a Vector Network Analyzer (VNA), as depicted in Fig. 15. The VNA ports are connected to frequency extenders to up-convert the signal to the D-band range. Both straight and S-bend waveguides are used to connect the extender ports to a CLAFSIW design. The VNA is calibrated with a standard TRL kit to remove the effects of the extenders and waveguides.

B. Straight CLAFSIW prototype analysis

In this section, we present an analysis of both simulated and the measured performance of the straight CLAFSIW design T_2 shown in Fig. 16, following its detailed study in Sect. II.

As shown in Fig. 17, the measurements of the transmission and reflection parameters have a fair agreement with the initial simulation. However, the transmission parameter is shifted to higher frequencies by almost $2.5\,$GHz. These differences indicate some manufacturing discrepancies, which we investigate with an optical microscope. A zoom of realized pads and vias is depicted in Fig. 18, with the dimensions clearly marked. The numerical ranges of dimensional errors are summarized in Table III. They effect the unit cell stopband and the matching of the vertical transition. Although they are in the acceptable range for standard PCB manufacturing, pad size is decreased by $15\,\%$ from $400\,\mu$m to $340\,\mu$m. This smaller size reduces the capacitance and shifts the stopband of the unit cell and the matching to higher frequencies as predicted by the analysis in Fig. 11. However, this difference is balanced with an increased substrate height by $7.5\,\%$ as shown in Fig. 5. This explains the close relation between our initial simulation and measurements. Although the edge clearance varies by up to 40%, thereby increasing the dielectric content within the structure, this variation has a negligible impact on overall performance. This is primarily because the dielectric losses are significantly less dominant than ohmic losses in this design, a detailed breakdown of which is provided in the loss decomposition analysis in the section III-C (see Table V).

Considering the results in Fig. 17, we note that the updated simulations assuming a $40\,\mu$m gap align closely the measurements. Due to the difficulties of measuring the exact gap size and its variance throughout the structure, we estimate with our simulations that its average value is in the range of $40 - 50\,\mu$m. Despite all the adjustments, transmission parameter in simulations is still higher than the measurements especially at lower frequencies. This could be explained with the matching being better at these frequencies.

Nevertheless, even with the standard PCB manufacturing tolerances and a cheap FR4 material, measurements confirm

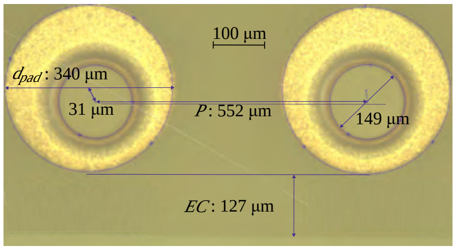

Fig. 18. Microscope image: Dimensional measurement of the prototype.

TABLE III
DIMENSIONAL DISCREPANCIES BETWEEN DESIGN AND PROTOTYPE

Parameters (μm)	Initial sim.	Prototype	Updated sim.
P	560	550–555	555
d_{pad}	400	330–342	340
EC	100	100–140	140
h	200	215	215
t	35	39	39
g	50	-	40

that our CLAFSIW design successfully operates in the target frequency band while maintaining a matching below -10 dB. Its transmission characteristics are also similar to the simulated ones, though it shows a 0.45 dB lower value on average between $134-148.5$ GHz compared to the simulation at $40\,\mu$m gap. At D-band frequencies, the skin depth ($\delta \approx 0.175\,\mu$m at 140 GHz) becomes comparable to the surface roughness of standard PCB copper foils. Therefore, to account for the additional loss, a parametric study of the effective conductivity (σ_{eff}) is performed at 40 μm gap in Fig. 19. The objective of the approach is to compensate the effects of surface roughness which is challenging to characterize directly. The parameter sweep identifies $5.8e6$ S/m of σ_{eff} providing a close alignment between the simulated model with the measurements.

Although calibrating the simulation model to explain prototype behavior is essential to understand the effects of design parameters, ensuring design reproducibility remains equally pivotal. As detailed in Table III, while the prototype dimensions exhibit systematic offsets from the initial simulation model, the statistical variance of the critical parameters across the board remains low. Consequently, pre-compensating the layout against the manufacturer's systematic offsets, similar to the approach in [29], can effectively ensure predictable operational responses during high-volume manufacturing. Regarding air gap size, replacing mechanical screw assembly with a PCB-compatible adhesive bonding process (e.g., lamination with a thin prepreg) suitable for mass production can stabilize the gap uniformity and align it closely with predicted values. Crucially, as demonstrated in Fig. 19, the proposed CLAFSIW maintains functional performance across a broader bandwidth than the band of interest. Further matching optimization and the incorporation of process-aware guard bands based on known statistical variations of the design parameters can enable stable performance and high reproducibility during mass production.

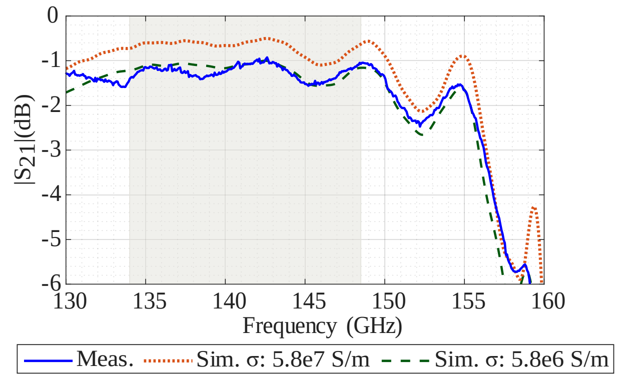

Fig. 19. Comparison of measured (meas.) and simulated (sim.) transmission performance of the design in Fig. 8 with standard (σ : $5.8e7$ S/m) and reduced (σ : $5.8e6$ S/m) copper conductivities and updated dimensions in Table III. The correlation of the effective conductivity model is shown to account for surface roughness effects. Grey rectangle highlights the $134-148.5$ GHz band.

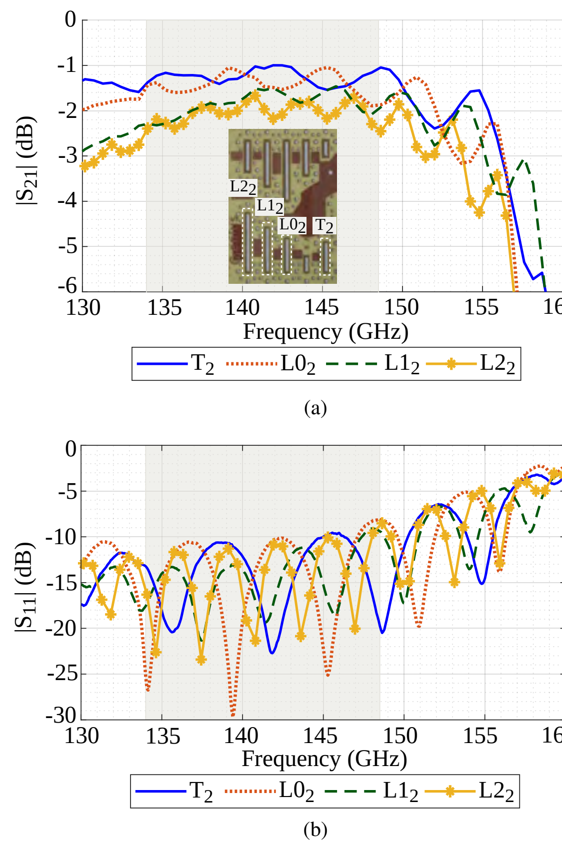

Fig. 20. Measurement comparison of transmission (a) and reflection (b) parameters of 2-row straight CLAFSIW designs from the shortest (T_2) to the longest ($L2_2$) length. Each of them are highlighted in the prototype image with white dashed rectangles. Grey rectangle shows the $134-148.5$ GHz band.

To further validate the scalability of our design, we compare the measured performance of two-row straight CLAFSIW lines under different lengths. In Fig. 20(a), the $|S_{21}|$ value decreases as line length increases, which demonstrates that our CLAFSIW design has stable performance regardless of its length. Fig. 20(b) confirms that all designs are well-matched, with an $|S_{11}|$ value below -10 dB across the desired fre-

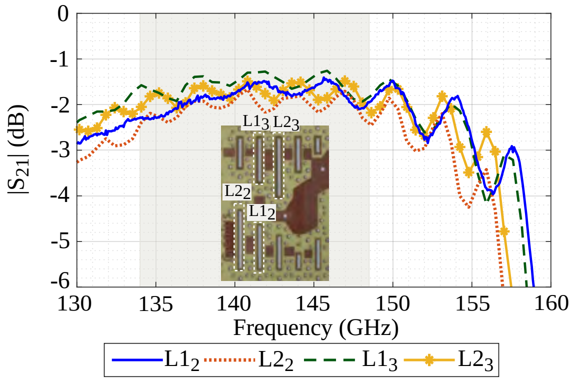

(a)

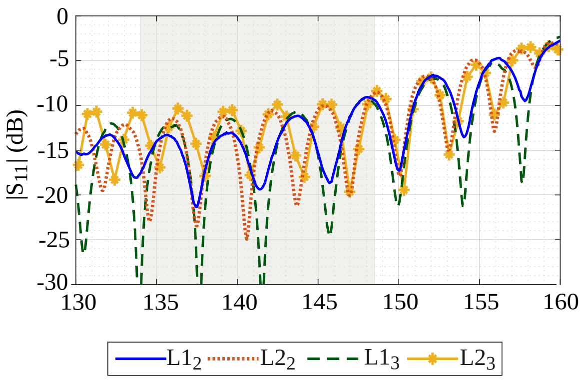

(b)

Fig. 21. Measurement comparison of transmission (a) and reflection (b) parameters of 2- and 3-row approach for L1 and L2 CLAFSIW designs. Inset prototype image with white dashed rectangles highlighting the analyzed designs. Grey rectangle shows the $134-148.5$ GHz band.

quency range. The average transmission loss per unit length is estimated by taking the difference between the $|S_{21}|$ of the longest (L2$_2$) and the shortest (T$_2$) design and averaging across the $134-148.5$ GHz range. We then divide the result by the length difference (21.28 mm) giving an estimated loss of 0.037 dB/mm. This differential technique reduces the matching effects and approaches to an isolated EBG performance which is used for comparison with TRL calibration in the next section.

Now, we test the wave confinement by comparing the measurements of L1$_2$ and L1$_3$ designs as well as L2$_2$ and L2$_3$ designs. They are well matched with $|S_{11}|$ below -10 dB within the band of interest. Even though 2-row designs have slightly less reflections, as shown in Fig. 21(a), adding a third row leads to a higher $|S_{21}|$, indicating improved wave confinement and reduced leakage from the waveguide. While this is a beneficial outcome for applications requiring higher confinement, the performance of 2-row designs are comparable. Given that our primary goal is a more compact design, we focus on the 2-row designs for the remainder of this paper.

C. Test under TRL de-embedding

In this section we apply the TRL de-embedding to accurately characterize losses by removing the effects of the vertical transition. We use the designs T$_2$, S$_2$ and L0$_2$ as thru, reflect and line standards respectively. L0$_2$ is made slightly longer than T$_2$ to achieve a phase value between $20-160$ degrees in the $134-148.5$ GHz band.

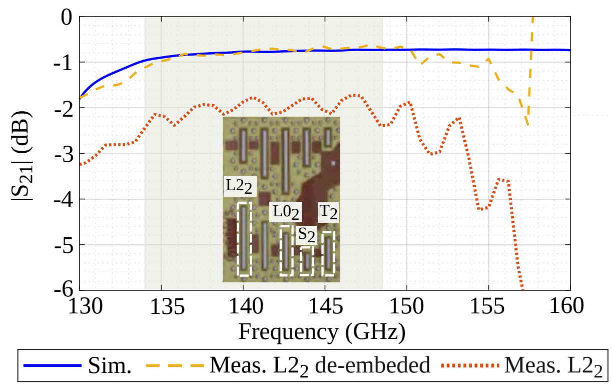

Fig. 22. Comparison between L2$_2$ measurements (meas.) and TRL de-embedded measurements and another simulation (sim.) model fed from sides, excluding vertical transition, at a length of 21.72 mm using updated dimensions in Table III and σ_{eff} : $5.8e6\ S/m$.

TABLE IV
TRANMISSION LOSS AS A FUNCTION OF FREQUENCY AFTER TRL DE-EMBEDING

f (GHz)	134	137	140	143	146	148.5
Loss (dB/mm)	0.052	0.039	0.037	0.034	0.033	0.030

Figure 22 depicts results before and after de-embedding of the design L2$_2$. The raw measurement (meas. L2$_2$) includes the cumulative loss of two vertical transitions and a total length of 42.56 mm ($20\lambda_c$). After de-embedding, the reference planes are shifted inside the waveguide channel, resulting in a length of 21.72 mm ($10.2\lambda_c$), thus exhibiting higher magnitude and significantly reduced oscillations as expected.

The measured transmission losses of CLAFSIW are presented in Table IV. They are performed by dividing the $|S_{21}|$ at each frequency point by the length of 21.72 mm. The design achieves a maximum loss of 0.052 dB/mm at 134 GHz and a minimum loss of 0.03 dB/mm at 148.5 GHz. The average of the measured loss in the operating band is 0.037 dB/mm. It has an excellent alignment with the value estimated in Sect. III-B, thereby confirming the performance of our concept using different de-embedding procedures.

In Fig. 22 we compare the measured de-embedded results with another CLAFSIW simulation at the same length using updated dimensions in Table III. The simulation results are obtained by exciting the waveguide from the sides as in Fig. 9 with $\sigma_{eff} = 5.8e6$ S/m. Using the effective conductivity model in Fig. 19 yields a great agreement with the de-embedded prototype. This provides further validation of our method as a mean of accounting for surface roughness.

Therefore, by using the same simulation environment, total loss is decomposed into ohmic, dielectric and leakage components and summarized in Table V. First, leakage loss is determined by modeling the conductors as Perfect Electric Conductors (PEC) within a lossless dielectric. Dielectric losses are then isolated by applying a lossy dielectric ($tan\delta = 0.01$) to the PEC model and subtracting the previously calculated

TABLE V
AVERAGE LOSS DECOMPOSITION AFTER TRL DE-EMBEDDING

Loss type	*Average* (dB/mm)	% of Total
Ohmic	0.029	78.4%
Dielectric	0.006	16.2%
Leakage	0.002	5.4%
Total	0.037	100%

TABLE VI
COMPARISON BETWEEN CONVENTIONAL TRANSMISSION TECHNOLOGIES

Tech.	Freq. (GHz)	Material	Loss (dB/mm)	Dim. (mm×mm)
Hollow waveguide [8]	110-170	Gold	0.0128 - 0.0081[1]	W: 1.651 H: 0.8255
Microstrip line [14]	135-145	Quartz Gold	0.29	W: 0.03 H: 0.127
SIW [20]	110-170	Ceramic copper	0.155	W: 0.625 H: 0.08
AFSIW [21]	115-155	Air Copper	0.07-0.08	W: 1.6 H: 0.3
MLW [29]	110-170	Air Silver	0.02	W: 1.65 H: 0.64
CLAFSIW (This work)	134-148.5	FR4 copper	0.037	W: 2.24 ∼ H: 0.37

leakage. Ohmic losses are derived by implementing the effective conductivity ($5.8e6$ S/m) in a lossless dielectric environment excluding leakage. The latter constitutes the vast majority of the total loss (78.4%) while dielectric loss accounts for only 16% demonstrating the advantage of the air-filled cavity despite the use of FR4. Notably, leakage from the EBG structure represents the minimum loss at merely 5.4% confirming the effectiveness of mushroom-type unit cells for D-band applications.

Here, we remark that a previous work [53] has demonstrated a viable array antenna performance using a PCB-based transmission line with a loss of 0.18 dB/mm at 150 GHz employing laser-drilling and specialized Megtron 7N substrate (ϵ_r: 3.2, tanδ: 0.003). In comparison, the proposed work achieves a loss that is nearly five times lower, significantly enhancing the efficiency of D-band interconnects despite the use of standard manufacturing techniques and materials. Additionally, Table VI compares our approach to several published conventional D-band technologies. It lists the type of technology, the operating band, materials, losses and the width (W) and height (H) of waveguide channels and microstrip line. Since these transmission lines utilize diverse materials making a direct comparison is difficult. Thus, we highlight the performance trade-offs in different transmission line approaches. By confining the waves within an air-filled cavity, the proposed CLAFSIW achieves lower insertion loss than microstrip lines on quartz or SIW

[1]Values assuming gold and a surface roughness factor of 1.5.

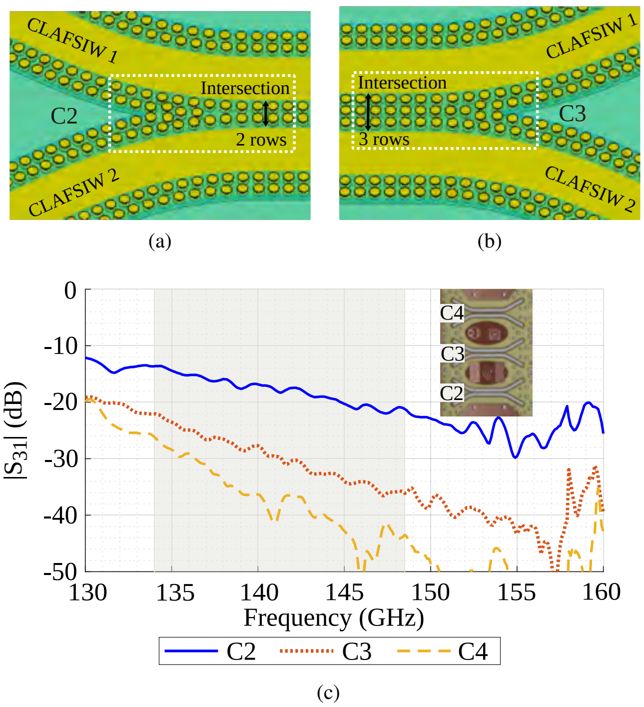

Fig. 23. (a) and (b) zoomed image of the intersection region (white dashed rectangle) of C2 and C3 designs, respectively. (c) Coupling comparison between de-embedded C2, C3 and C4 designs. Grey rectangle shows the $134-148.5$ GHz band.

structures on ceramic substrates, despite being fabricated on lossy FR4. Our design is positioned between AFSIW and a silver plated multi-layer waveguide (MLW). Although a fully metallic MLW approach is more advantageous in terms of losses, our approach prioritizes ease of integration to PCB assemblies using high volume processes and economically scalable materials without significantly compromising D-band performance.

In the context of automotive radar, we benchmark this work against a CNC-milled metallic ridge gap waveguide designed for Launcher in Package (LiP) applications [45]. The latter achieves an insertion loss of 0.0186 dB/mm at 77 GHz. Considering that conductor losses inherently scale with frequency, the 0.037 dB/mm loss achieved by our proposed design at 140 GHz is highly comparable. Therefore our FR4-based PCB solution provides an industry standard efficiency while simultaneously meeting the critical requirements of cost-effectiveness and scalability for D-band automotive radars.

D. Coupling suppression

We now proceed to investigate the coupling between two intersecting 2-row CLAFSIW designs. The analysis focus particularly on the intersection region where the amount of unit cell rows varies as illustrated in the images in Figs. 23(a) and 23(b). We measure the $|S_{31}|$ parameter highlighting the coupling between the Port 1 and Port 3, with matched loads at Ports 2 and 4. Here we apply the TRL de-embedding to remove the mismatch effects and purely characterize the suppression of the coupling with respect to increasing number of unit cell rows at the intersection. The results of this approach are presented in Fig. 23(c). We observe that the coupling linearly decreases in dB scale with each additional row contributing to a more effective isolation. The coupling is substantially reduced, below $-13.6\,$dB, $-22\,$dB and $-26\,$dB for C2, C3 and C4 configurations, respectively. These results demonstrate the EBG structure robustness in reducing signal interference, even when accounting manufacturing discrepancies in Table III.

IV. Conclusion and perspectives

In this paper we demonstrated for the first time a CLAFSIW concept targeting the $134 - 148.5\,$GHz frequency range. The proposed approach proves that a PCB-based solution can effectively operate at D-band while eliminating the need for galvanic contact. The double-layer design is compatible with standard FR4 PCB technology ensuring simplified fabrication, and scalable for mass production. The double side mushroom unit cell, analyzed with MMTMM, maintains a stopband between $127 - 169.7\,$GHz with a peak attenuation in the target band. The E-bend vertical transition ensures an easy integration with microchips based on waveguide launchers and provides an $|S_{11}|$ below $-10\,$dB. Prototype measurements demonstrated valid and satisfactory results that met simulation expectations, confirming a design specifically optimized to maintain performance despite fabrication inaccuracies and sensitivity to the pad size, air-gap and substrate height. Applying a TRL de-embedding showed $0.037\,$dB/mm transmission losses on average, providing a competitive performance compared to conventional technologies at D-band. We also showed that the coupling between adjacent structures can be reduced below $-26\,$dB. Overall, our research demonstrated a novel, low-loss and cost-effective transmission line technology capable of confining high-frequency waves, using cheap, lossy materials and standard manufacturing. This significant practical advantage, paves the way for its commercial viability in diverse D-band applications in automotive industry.

V. Acknowledgments

We would like to thank Dr. Peter Uhlig from IMST GmbH for the dimensional measurements and constructive criticism of the manuscript.

References

[1] I. Bilik, O. Longman, S. Villeval, and J. Tabrikian, “The Rise of Radar for Autonomous Vehicles: Signal Processing Solutions and Future Research Directions,” *IEEE Signal Processing Magazine*, vol. 36, no. 5, pp. 20–31, 2019.

[2] S. S. Ram, “Fusion of Inverse Synthetic Aperture Radar and Camera Images for Automotive Target Tracking,” *IEEE Journal of Selected Topics in Signal Processing*, vol. 17, no. 2, pp. 431–444, 2023.

[3] IEEE, “Heterogeneous Integration Roadmap, Chapter 5: Automotive,” IEEE Electronics Packaging Society (EPS), Tech. Rep., 2021. [Online]. Available: https://eps.ieee.org/technology

[4] K. Ramasubramanian and K. Ramaiah, “Moving from Legacy 24 GHz to State-of-the-Art 77-GHz Radar,” *ATZelektronik worldwide*, vol. 13, no. 3, pp. 46–49, Jun 2018. [Online]. Available: https://doi.org/10.1007/s38314-018-0029-6

[5] A. Bazzi, F. Miccoli, Z. Wu, F. Cuccoli, and V. Martinez, “A Tool for the Statistical Investigation of the Automotive Radar Interference,” in *2024 4th URSI Atlantic Radio Science Meeting (AT-RASC)*, 2024, pp. 1–4.

[6] V. Martinez, A. Filippi, and M. Vlot, “D-band vehicular radars regulatory status,” in *2024 21st European Radar Conference (EuRAD)*, 2024, pp. 276–279.

[7] S. Kueppers, T. Jaeschke, N. Pohl, and J. Barowski, “Versatile 126-182 GHz UWB D-Band FMCW Radar for Industrial and Scientific Applications,” *IEEE Sensors Letters*, vol. 6, no. 1, pp. 1–4, 2022.

[8] Virginia Diodes, Inc. (VDI), “VDI Waveguide Band Designations,” Application Note, Virginia Diodes, Inc., Jun. 2010, accessed: May 11, 2026. [Online]. Available: https://vadiodes.com/wp-content/uploads/2009/10/waveguidechart200908.pdf

[9] P.-S. Kildal, E. Alfonso, A. Valero-Nogueira, and E. Rajo-Iglesias, “Local Metamaterial-Based Waveguides in Gaps Between Parallel Metal Plates,” *IEEE Antennas and Wireless Propagation Letters*, vol. 8, pp. 84–87, 2009.

[10] W. Y. Yong, A. Vosoogh, A. Bagheri, C. Van De Ven, A. Hadaddi, and A. A. Glazunov, “An Overview of Recent Development of the Gap-Waveguide Technology for mmWave and Sub-THz Applications,” *IEEE Access*, vol. 11, pp. 69 378–69 400, 2023.

[11] T. Skaik, M. Salek, P. Hunyor, H. Wang, P. G. Huggard, P. F. Wilson, M. A. Williams, and Y. Wang, “Evaluation of 3-D Printed Monolithic G-Band Waveguide Components,” *IEEE Transactions on Components, Packaging and Manufacturing Technology*, vol. 13, no. 2, pp. 240–248, 2023.

[12] M. D’Auria, W. J. Otter, J. Hazell, B. T. W. Gillatt, C. Long-Collins, N. M. Ridler, and S. Lucyszyn, “3-D Printed Metal-Pipe Rectangular Waveguides,” *IEEE Transactions on Components, Packaging and Manufacturing Technology*, vol. 5, no. 9, pp. 1339–1349, 2015.

[13] Y. Zhang, J. Zhang, R. Yue, and Y. Wang, “Loss Analysis of Thin Film Microstrip Line With Low Loss at D Band,” *Journal of Lightwave Technology*, vol. 39, no. 8, pp. 2421–2430, April 2021.

[14] G. Guo, T. Zhang, J. Zeng, Z. Yang, L. Yue, and Y. Wei, “Investigation and Fabrication of the Printed Microstrip Meander-Line Slow-Wave Structures for D-Band Traveling Wave Tubes,” *IEEE Transactions on Electron Devices*, vol. 69, no. 9, pp. 5229–5234, 2022.

[15] J. Xiao, X. Li, Z. Qi, and H. Zhu, “140-GHz TE_{340} -Mode Substrate Integrated Cavities-Fed Slot Antenna Array in LTCC,” *IEEE Access*, vol. 7, pp. 26 307–26 313, 2019.

[16] Z.-W. Miao, Z.-C. Hao, G. Q. Luo, L. Gao, J. Wang, X. Wang, and W. Hong, “140 GHz High-Gain LTCC-Integrated Transmit-Array Antenna Using a Wideband SIW Aperture-Coupling Phase Delay Structure,” *IEEE Transactions on Antennas and Propagation*, vol. 66, no. 1, pp. 182–190, 2018.

[17] J. Xu, Z. N. Chen, X. Qing, and W. Hong, “140-GHz Planar Broadband LTCC SIW Slot Antenna Array,” *IEEE Transactions on Antennas and Propagation*, vol. 60, no. 6, pp. 3025–3028, 2012.

[18] A. Altaf and M. Seo, “SIW Based D-Band Single and 2 x 2 MIMO Elliptically Tapered Slot Antenna,” *IEEE Access*, vol. 11, pp. 87 270–87 278, 2023.

[19] Y. Su, Y. Chen, Z. Wu, Z. He, Z. Niu, F. Xiong, X. Jie, C. Wang, and B. Zhang, “140 GHz Slow-Wave Structure Loaded SIW Miniaturized Butler Matrix for Multibeam Application,” in *2024 IEEE International Symposium on Radio-Frequency Integration Technology (RFIT)*, 2024, pp. 1–3.

[20] N. Aslani-Amoli, M. u. Rehman, L. N. Vijay Kumar, A. Moradinia, F. Liu, M. Swaminathan, C.-G. Zhuang, R. Vaddi, S.-H. Seok, and C. Kim, “Ultralow-Loss Substrate-Integrated Waveguides in Alumina Ribbon Ceramic Substrates for 75-170 GHz Wireless Applications,” *IEEE Microwave and Wireless Technology Letters*, vol. 33, no. 10, pp. 1415–1418, 2023.

[21] S. Sinha, H. Trischler, I. Ocket, and E. Schaffler, “D-Band Air-Filled Substrate Integrated Waveguide (AFSIW) and Broadband Stripline to AFSIW Launcher Embedded in Multi-Layer PCBs,” *IEEE Microwave and Wireless Technology Letters*, vol. 33, no. 6, pp. 795–798, 2023.

[22] M. u. Rehman, L. N. V. Kumar, S. Erdogan, and M. Swaminathan, “Air-Filled SIWs Using Laminate Dielectrics on Glass Substrate for D-Band Applications,” *IEEE Transactions on Components, Packaging and Manufacturing Technology*, vol. 14, no. 1, pp. 98–105, 2024.

[23] D. Zarifi, A. Farahbakhsh, and A. U. Zaman, “A Gap Waveguide-Based D-Band Slot Array Antenna With Interdigital Feed Network,” *IEEE Transactions on Antennas and Propagation*, vol. 71, no. 9, pp. 7124–7131, 2023.

[24] J. Liu, A. U. Zaman, and J. Yang, “Two Types of High Gain Slot Array Antennas based on Ridge Gap Waveguide in the D-Band,” in *2019 IEEE-APS Topical Conference on Antennas and Propagation in Wireless Communications (APWC)*, 2019, pp. 075–078.

[25] A. Vosoogh, A. U. Zaman, and V. Vassilev, “Wideband cavity-backed slot subarray with gap waveguide feed-network for D-band applications,”

in *2017 11th European Conference on Antennas and Propagation (EUCAP)*, 2017, pp. 207–209.

[26] A. Farahbakhsh, D. Zarifi, and A. Uz Zaman, "D-Band High-Gain Planer Slot Array Antenna Using Gap Waveguide Technology," *IEEE Transactions on Antennas and Propagation*, vol. 73, no. 1, pp. 594–599, 2025.

[27] P. Boe, K. Reuter, D. Miek, T. Studnitzky, C. Zhong, T. Weißgärber, and M. Höft, "High-Precision Additive Manufacturing of Groove Gap Waveguide Filters in D-Band," in *2024 IEEE Asia-Pacific Microwave Conference (APMC)*, 2024, pp. 405–407.

[28] J. Zhai, F. Ren, J. Li, and H. Xu, "A D-band Contactless Wideband Transition of Ridge Gap Waveguide and Microstrip," in *2024 IEEE MTT-S International Microwave Workshop Series on Advanced Materials and Processes for RF and THz Applications (IMWS-AMP)*, 2024, pp. 1–3.

[29] A. Vosoogh, H. Zirath, and Z. S. He, "Novel Air-Filled Waveguide Transmission Line Based on Multilayer Thin Metal Plates," *IEEE Transactions on Terahertz Science and Technology*, vol. 9, no. 3, pp. 282–290, 2019.

[30] Gapwaves AB, "Gapwaves Waveguide Technology." [Online]. Available: https://gapwaves.com/waveguide-technology/

[31] K. Aktas, M. Petek, E. Tolin, S. Bruni, and F. Vipiana, "Cost Effective PCB Gap Waveguide Based on Broken Glide Symmetry," in *2025 19th European Conference on Antennas and Propagation (EuCAP)*, 2025, pp. 1–4.

[32] F. Ghasemifard, F. Mesa, G. Valerio, and O. Quevedo-Teruel, "Propagation Characteristics in Substrate Integrated Holey Metasurfaces," in *2020 14th European Conference on Antennas and Propagation (EuCAP)*, 2020, pp. 1–4.

[33] B. Fischer, J. Sarrazin, and G. Valerio, "Glide-Symmetric Reconfigurable Substrate-Integrated Holey Waveguide," in *2024 18th European Conference on Antennas and Propagation (EuCAP)*, 2024, pp. 1–4.

[34] D. Sievenpiper, L. Zhang, R. Broas, N. Alexopolous, and E. Yablonovitch, "High-impedance electromagnetic surfaces with a forbidden frequency band," *IEEE Transactions on Microwave Theory and Techniques*, vol. 47, no. 11, pp. 2059–2074, 1999.

[35] N. Bayat-Makou and A. A. Kishk, "Contactless Air-Filled Substrate Integrated Waveguide," *IEEE Transactions on Microwave Theory and Techniques*, vol. 66, no. 6, pp. 2928–2935, 2018.

[36] C. Segura-Gómez, Á. Palomares-Caballero, A. Alex-Amor, C. Molero, and P. Padilla, "Air-SIW Unit Cell with Glide-Symmetric Structures," in *2023 17th European Conference on Antennas and Propagation (EuCAP)*, 2023, pp. 1–4.

[37] X. Zhao, Z. Yan, Y. Bi, F. Fan, D. Sun, B. Wei, E. Wang, Z. Wang, and R. Li, "High-Order Resonating Cavity-Backed Slot Antenna Array Based on Contactless Air-Filled Substrate-Integrated Waveguide and Transition to Inverted Grounded Coplanar Gap Waveguide," *IEEE Transactions on Antennas and Propagation*, vol. 72, no. 12, pp. 8991–9001, 2024.

[38] A. Amirkabiri, D. Idoko, G. E. Bridges, and B. Kordi, "Contactless Air-Filled Substrate-Integrated Waveguide (CLAF-SIW) Resonator for Wireless Passive Temperature Sensing," *IEEE Transactions on Microwave Theory and Techniques*, vol. 70, no. 7, pp. 3724–3731, 2022.

[39] M. Sharifi Sorkherizi and A. A. Kishk, "Self-Packaged, Low-Loss, Planar Bandpass Filters for Millimeter-Wave Application Based on Printed Gap Waveguide Technology," *IEEE Transactions on Components, Packaging and Manufacturing Technology*, vol. 7, no. 9, pp. 1419–1431, 2017.

[40] A. Ugle, M. Casaletti, M. A. Campo, S. Bruni, and G. Valerio, "Stacked Multi-Via Mushroom-Type EBG Structures With Glide Symmetry," in *2025 19th European Conference on Antennas and Propagation (EuCAP)*, 2025, pp. 1–5.

[41] Z. S. He, A. Hassona, A. Pérez-Ortega, and H. Zirath, "A Compact PCB Gasket for Waveguide Leakage Suppression at 110-170 GHz," in *2020 IEEE/MTT-S International Microwave Symposium (IMS)*, 2020, pp. 888–891.

[42] D. Schwarz, N. Riese, A. Dürr, and C. Waldschmidt, "A Broadband Multilayer Vertical Transition at 79 GHz Employing FR4 as Core Material," in *2021 51st European Microwave Conference (EuMC)*, 2022, pp. 700–703.

[43] D. Schwarz, N. Riese, I. Dorsch, and C. Waldschmidt, "System Performance of a 79 GHz High-Resolution 4D Imaging MIMO Radar With 1728 Virtual Channels," *IEEE Journal of Microwaves*, vol. 2, no. 4, pp. 637–647, 2022.

[44] H. U. R. Mohammed, "Advancements in mmWave Technology: Launch on Package for Automotive Radars," Texas Instruments, White Paper SWRA801, Jan 2024. [Online]. Available: https://www.ti.com/lit/wp/swra801/swra801.pdf

[45] Q. Ren, C. Bencivenni, G. Carluccio, H. T. Shivamurthy, A. De Graauw, F. Jansen, J. Yang, and A. U. Zaman, "Gapwaveguide Automotive Imaging Radar Antenna With Launcher in Package Technology," *IEEE Access*, vol. 11, pp. 37 483–37 493, 2023.

[46] Q. Chen, F. Mesa, X. Yin, and O. Quevedo-Teruel, "Accurate Characterization and Design Guidelines of Glide-Symmetric Holey EBG," *IEEE Transactions on Microwave Theory and Techniques*, vol. 68, no. 12, pp. 4984–4994, 2020.

[47] M. Petek, J. Rico-Fernández, J. A. T. Vásquez, G. Valerio, F. Mesa, O. Quevedo-Teruel, and F. Vipiana, "Numerical Modeling of Higher-Symmetric Periodic Structures With a Hexagonal Lattice," *IEEE Transactions on Antennas and Propagation*, vol. 73, no. 3, pp. 1650–1661, 2025.

[48] F. Giusti, Q. Chen, F. Mesa, M. Albani, and O. Quevedo-Teruel, "Efficient Bloch Analysis of General Periodic Structures With a Linearized Multimodal Transfer-Matrix Approach," *IEEE Transactions on Antennas and Propagation*, vol. 70, no. 7, pp. 5555–5562, 2022.

[49] F. Mesa, G. Valerio, R. Rodríguez-Berral, and O. Quevedo-Teruel, "Simulation-Assisted Efficient Computation of the Dispersion Diagram of Periodic Structures: A comprehensive overview with applications to filters, leaky-wave antennas and metasurfaces," *IEEE Antennas and Propagation Magazine*, vol. 63, no. 5, pp. 33–45, 2021.

[50] N. P. Gaunkar, G. Dogiamis, T. Kamgaing, A. Elsherbini, and J. Swan, "Multi-layer FCCSP organic packaging for D-band millimeter wave applications," in *2022 IEEE 72nd Electronic Components and Technology Conference (ECTC)*, 2022, pp. 365–370.

[51] Panasonic Industry Co., Ltd., "Halogen Free R-1566," 2022, accessed: May 11, 2026. [Online]. Available: https://industrial.panasonic.com/ww/products/pt/halogen-free/hfreer1566

[52] IMST GmbH, "EMPIRE - Extremely fast 3D simulator for electromagnetic fields," 2026, accessed: May 11, 2026. [Online]. Available: https://empire.de/

[53] A. Lamminen, J. Säily, J. Ala-Laurinaho, J. de Cos, and V. Ermolov, "Patch Antenna and Antenna Array on Multilayer High-Frequency PCB for D-Band," *IEEE Open Journal of Antennas and Propagation*, vol. 1, pp. 396–403, 2020.

Kaan Aktaş Kaan Aktaş (Student Member, IEEE) earned his B.Sc. and M.Sc. degree in electrical engineering from Sorbonne University, Paris, France in 2021 and 2023 respectively. During his academic career, he specialized in electromagnetic theory and microwave engineering. He is currently pursuing his PhD at Politecnico di Torino, Italy and at IMST GmbH, Germany under the GENIUS program of Marie Curie doctoral network. His research interests include metasurfaces, higher symmetric periodic structures, microwave circuits and radar systems.

Martin Petek Martin Petek (Member, IEEE) received his B.Sc. degree in electrical engineering from University of Ljubljana in 2017 and his M.Sc. in Electrophysics from KTH Royal Institute of Technology in 2020. He obtained his PhD degree (cum laude) from Politecnico di Torino, Torino, Italy in 2025. He is currently at Politecnico di Torino in Department of Electronics and Telecommunications as a postdoctoral researcher. His current research interests include numerical techniques, periodic structures, and higher symmetries.

Enrico Tolin Enrico Tolin received the M.Sc. degree in electronic engineering from the Università degli Studi di Padova, Padua, Italy, in 2008, and the Ph.D. degree in Electrical, Electronics and Communications Engineering from the Politecnico di Torino, Torino, Italy, in 2020. From 2010 to 2014, he was a Research and Development Engineer with Calearo Antenne SPA, Vicenza, Italy. Since 2014, he has been a part of the Antennas and EM Modeling Group, IMST GmbH, Kamp-Lintfort, Germany. His current research interests include the design of reconfigurable antennas and systems, integrated antennas, antenna arrays, active and passive circuits, and low-noise amplifiers.

Simona Bruni Simona Bruni (Member, IEEE) was born in Civitavecchia, Italy. She received the M.S. degree in telecommunication engineering and the Ph.D. degree in electromagnetics from the University of Siena, Siena, Italy, in 2002 and 2006, respectively.

From 2005 to 2007, she was a researcher financed and hosted by the Defense, Security and Safety Institute, Netherlands Organization for Applied Scientific Research (TNO), The Hague, The Netherlands. From 2007 to 2013, she worked as a Research and Development Antenna Engineer with the Calearo Advanced Technology (CAT) Department, Calearo SPA (later acquired by MTA), Vicenza, Italy. Since 2013, she has been working as a Research and Development Antenna Engineer at the Antenna Front-Ends Team, Antennas and EM Modeling Department, IMST GmbH, Kamp-Lintfort, Germany. She co-authored the article that received the Best Applied Technology Antenna Paper Award from European Conference on Antennas and Propagation (EuCAP) in 2023. Since 2026, she has been serving as a member of the Advisory Board for the Department of Electronics and Telecommunications (DET), Politecnico di Torino, Turin, Italy. Since 2026, she has been the Technical Co-Director of Sub-THz antenna systems with IMST GmbH. Her research is dedicated to advanced integrated antennas, high-frequency antenna arrays, and front-end designs, with a strong focus on communication, sensing, and automotive systems.

Jorge A. Tobón Vásquez Jorge A. Tobón Vásquez received the Degree in electronics engineering from the Universidad de Antioquia, Colombia, in 2010; the master's degree and the Ph.D in electronics and telecommunication from the Politecnico di Torino, Italy, in 2010 and 2014, respectively. Since 2024 he has also worked in Wavision S.r.l. (Politecnico di Torino spin-off). His main research activities correspond to modelling, designing, and analyzing systems for microwave imaging applications, and the numerical modelling of complex and nonhomogeneous media propagation. In 2018 received the "Premio Latmiral," an award granted by the Italian Society of Electromagnetism (SIEM). In 2020 he received the URSI General Assembly Scientific Symposium (GASS) Young Scientist Award (YSA) and the Sorrentino URSI Italy National Meeting Young Scientist Paper Award.

Francesca Vipiana Francesca Vipiana (Senior Member, IEEE) received the Laurea and Ph.D. degrees in electronic engineering from the Politecnico di Torino, Torino, Italy, in 2000 and 2004, respectively, with doctoral research carried out partly at the European Space Research Technology Center, Noordwijk, The Netherlands. From 2005 to 2008, she was a Research Fellow with the Department of Electronics, Politecnico di Torino. From 2009 to 2012, she was the Head of the Antenna and EMC Laboratory, Istituto Superiore Mario Boella, Torino. Since 2012, she has been an Assistant Professor with the Department of Electronics and Telecommunications, Politecnico di Torino, where she has been an Associate Professor since 2014 and a Full Professor since 2021.

Her main research activities concern numerical techniques based on integral equations and method of moments, with a focus on multiresolution and hierarchical schemes, domain decomposition, preconditioning and fast solution methods, advanced quadrature integration schemes, and analysis of glide-periodic structures. Moreover, her research interests include the modeling, design, realization and testing of microwave imaging and sensing systems for medical and industrial applications.

She received the Lot Shafai Mid-Career Distinguished Award from the IEEE Antennas and Propagation Society (AP-S) in 2017, the Best Paper Award at the Spanish URSI Symposium in 2023, and the Best Electromagnetics Paper Award at the 20th European Conference on Antennas and Propagation (EuCAP) in 2026. She was an Associate Editor of the IEEE Transactions on Antennas and Propagation (2018-2024) and the founder and responsible of the Women in Engineering Column in the IEEE Antennas and Propagation Magazine (2019-2024). She is a member of the EurAAP Board of Directors and the Vice-Chair of the IEEE AP-S Expanding Collaboration & Engagement (ECE) committee.